ORIGINAL ARTICLE

Radiomics analysis of [18F]FDG PET/CT for microvascular invasion and prognosis prediction in very-early- and early-stage hepatocellular carcinoma

Youcai Li[1] · Yin Zhang[2] · Qi Fang[1] · Xiaoyao Zhang[1] · Peng Hou[1] · Hubing Wu[2] · Xinlu Wang[1]

Abstract

As a reliable preoperative predictor for microvascular invasion (MVI) and disease-free survival (DFS) is lacking, we developed a radiomics nomogram of [18F]FDG PET/CT to predict MVI status and DFS in patients with very-early- and early-stage (BCLC 0, BCLC A) hepatocellular carcinoma (HCC).

Methods Patients ($N = 80$) with BCLC0-A HCC who underwent [18F]FDG PET/CT before surgery were enrolled in this retrospective study and were randomized to a training cohort and a validation cohort. Texture features from patients obtained using Lifex software in the training cohort were subjected to LASSO regression to select the most useful predictive features of MVI and DFS. Then, the radiomics nomogram was constructed using the radiomics signature and clinical features and further validated.

Results To predict MVI, the [18F]FDG PET/CT radiomics signature consisted of five texture features from the PET and six texture features from CT. The signature was significantly associated with MVI status in the training cohort ($P = 0.001$). None of the clinical features was independent predictors for MVI status ($P > 0.05$). The area under the curve value of the M-PET/CT model was 0.891 (95% CI: 0.799–0.984) in the training cohort and showed good discrimination and calibration. To predict DFS, the [18F]FDG PET/CT radiomics nomogram (D-PET/CT model) and a clinicopathologic nomogram were built in the training cohort. The D-PET/CT model, which integrated the D-PET/CT radiomics signature with INR and TB, provided better predictive performance (C-index: 0.831, 95% CI: 0.761–0.900) and larger net benefits than the simple clinical model, as determined by decision curve analyses.

Conclusion The newly developed [18F]FDG PET/CT radiomics signature was an independent biomarker for the estimation of MVI and DFS in patients with very-early- and early-stage HCC. Moreover, PET/CT nomogram, which incorporated the radiomics signature of [18F]FDG PET/CT and clinical risk factors in patients with very-early- and early-stage HCC, performed better for individualized DFS estimation, which might enable a step forward in precise medicine.

Keywords Hepatocellular carcinoma · MVI · DFS · Radiomics · [18F]FDG PET/CT model

---

Youcai Li and Yin Zhang contributed equally to this work.

This article is part of the Topical Collection on Hematology

✉ Hubing Wu
wuhbym@163.com

✉ Xinlu Wang
71lu@163.com

1 Department of Nuclear Medicine, The First Affiliated Hospital of Guangzhou Medical University, No. 151, Yanjiang Road, Yuexiu District, Guangzhou 510000, Guangdong, China

2 Nanfang PET Center, Nanfang Hospital, Southern Medical University, 1838 Guangzhou Avenue North, Guangzhou 510515, Guangdong Province, China

Introduction

Hepatocellular carcinoma (HCC) is a common malignancy that ranks as the fourth leading cause of cancer-related deaths worldwide [1]. Although most patients present with advanced disease when first seen by a physician, some patients are actually diagnosed at the very early and early stage (BCLC 0-A) [2]. Partial hepatectomy is the best modality for treating these patients [3]. However, it was found that the prognosis of very-early- and early-stage HCC after hepatic segmentectomy varied [4]. In some patients, the disease progresses slowly and has along disease-free survival (DFS), while in some patients, the tumors recur and progress quickly [4]. The varied prognosis may have resulted from the high heterogeneity of the

tumors [5, 6]. Some tumors manifest as having highly aggressive characteristics, and the patients have a poor prognosis. Alternatively, some tumors appear as low-grade tumors with slow growth.

Microvascular invasion (MVI) is defined as the invasion of HCC cells to the microvascular of peritumoral tissues, which can only be visible on the pathological section under the microscopy after operation. It is one of the pathological features reflecting the invasiveness of the tumor. Highly aggressive HCC often exhibits obvious MVI, while low-grade HCC often appears with no MVI. HCC with MVI has a 4.4-fold higher risk of tumor recurrence, and the patient has a much shorter DFS [7]. Therefore, MVI is recognized as an important prognostic factor in HCC [8–10]. Preoperative prediction of MVI in HCC using noninvasive imaging modalities, such as β-2-[^{18}F] fluoro-2-deoxy-D-glucose positron emission tomography/computed tomography ([^{18}F]FDG PET/CT), magnetic resonance imaging(MRI), computed tomography(CT), or ultrasound (US) [11–13], has attracted clinical interest.

[^{18}F]FDG PET/CT is an integrated imaging modality of PET and CT, which is always used for evaluating and staging the malignant tumors before surgery, including HCC [14, 15]. The semi-quantitative indices such as maximum standardized uptake value (SUV$_{max}$) and TLR (tumor-to-liver ratio) on PET images [16] are often used to quantify tumor glucose metabolism, which may have a positive relationship with MVI and the prognosis of HCC patient [17, 18]. Pseudocapsule sign of the lesion on CT was also reported to prompt the low grade of the tumor. On the other hand, fuzzy and irregular boundary of the lesion often indicates the invasiveness of the tumor, which often indicates MVI. However, both the SUV$_{max}$ and TLR can only provide the gross glucose metabolism of the tumor, but not reflect the subtle heterogeneity of metabolism in different parts of the tumor. In addition, edge information of the lesion analyzed by visual assessment has great inter-observer variability.

Radiomics is an emerging method for imaging analysis using algorithms or statistical analysis tools to capture distinct phenotypic differences of tumors from diagnostic images. The radiomics features can provide a great deal of information beyond analysis with the naked eye and can sensitively determine the subtle heterogeneity of the morphology and function among different parts within the tumor at the cellular level [19]. Radiomics has shown its powerful potential in diagnosis and prognosis predicting in some tumors based on analysis of image features extracted from CT, MRI, or PET/CT. To the best of our knowledge, no article has introduced radiomics analysis to predict MVI and prognosis in very-early- and early-stage HCC. Therefore, in this paper, we investigate the capacity of the radiomics signature extracted from

preoperative [^{18}F]FDG PET/CT to predict MVI and DFS in patients with very-early- and early-stage HCC.

Materials and methods

Patients

Ethical approval was waived by the local Ethics Committee of Guangzhou Medical University and Southern Medical University in view of the retrospective nature of the study.

We retrospectively reviewed data from patients with histologically confirmed very-early- and early-stage (BCLC0, BCLCA) HCC who underwent radical surgical resection between March 2013 and April 2019 at the First Affiliated Hospital of Guangzhou Medical University and Southern Medical University Nanfang Hospital. The tumors were staged according to the Barcelona Clinic Liver Cancer (BCLC) system. Inclusion criteria included (1) pathologically confirmed primary HCC, (2) [^{18}F]FDG PET/CT performed less than 2 weeks prior to surgery, (3) availability of follow-up data and clinical-pathologic characteristics, and (4) no history of preoperative anti-cancer treatment. Patients were excluded if he/she had multiple primary cancers or had a previous history of cancer. The endpoint of this study was DFS calculated from the day of surgery to the date of disease progression (locoregional recurrences or metastases), death from any cause (censored), or the date of the last follow-up visit (censored). Local recurrence and distant metastasis were diagnosed based on clinical symptoms, physical examination, AFP essay, and imaging findings including chest X-ray, abdominal ultrasound, enhanced contrast CT or MRI, whole-body bone scan, and PET/CT. A total of 80 consecutive patients who met the criteria were enrolled and divided into two cohorts (training and validation cohort) with a ratio of 5:3 using computer-generated random numbers. As a result, 50 patients were allocated to the training cohort, and 30 patients were allocated to the independent validation cohort. Clinical information is presented in Table 1. Of these 80 patients, 63 patients underwent isolated enhanced CT, 7 had isolated MRI examinations, and 4 underwent both CT and MRI prior to radical surgical resection.

Histopathology

All patients underwent radical surgical resection within 2 weeks of [^{18}F]FDG PET/CT examination. All surgical specimens were reviewed by a pathologist with more than 10 years of experience in liver pathology, in particular to estimate the presence of MVI. MVI was defined as the presence of tumor in a portal vein, hepatic

Table 1 Clinical and histopathological characteristics and imaging indicators of patients with very early and early HCC in the training and validation cohort

Variables	Training cohort (n = 50)		Validation cohort (n = 30)		P
	MVI−	MVI+	MVI−	MVI+	
Age (years)					0.226
≤ 50	12 (60.0)	8 (40.0)	2 (25.0)	6 (75.0)	
> 50	16 (53.3)	14 (46.7)	14 (63.6)	8 (36.4)	
Sex					1.000
Male	25 (54.3)	21 (45.7)	15 (55.6)	12 (44.4)	
Female	3 (75.0)	1 (25.0)	1 (33.3)	2 (66.7)	
Diameter (cm)					0.664
≤ 3	14 (73.7)	5 (26.3)	8 (80.0)	2 (20.0)	
3–5	6 (50.0)	6 (50.0)	5 (50.0)	5 (50.0)	
> 5	8 (42.1)	11 (57.9)	3 (30.0)	7 (70.0)	
HBV infection					0.518
Absent	2 (33.3)	4 (66.7)	3 (50.0)	3 (50.0)	
Present	26 (59.1)	18 (40.9)	13 (54.2)	11 (45.8)	
Child-Pugh					0.248
A	24 (55.8)	19 (44.2)	16 (55.2)	13 (44.8)	
B	4 (57.1)	3 (42.9)	0 (0.0)	1 (100)	
Cirrhosis					0.538
Absent	8 (53.3)	7 (46.7)	5 (45.5)	6 (54.5)	
Present	20 (57.1)	15 (42.9)	11 (57.9)	8 (42.1)	
Tumor differentiation					1.000
Well-moderately	23 (54.8)	19 (45.2)	14 (56.0)	11 (44.0)	
Poorly	5 (62.5)	3 (37.5)	2 (40.0)	3 (60.0)	
BCLC stage					0.447
0	6 (60.0)	4 (40.0)	3 (75.0)	1 (25.0)	
A	22 (55.0)	18 (45.0)	13 (50.0)	13 (50.0)	
ALT (U/L)					0.365
≤ 50	22 (57.9)	16 (42.1)	10 (50.0)	10 (50.0)	
> 50	6 (50.0)	6 (50.0)	6 (60.0)	4 (40.0)	
AST (U/L)					1.000
≤ 40	17 (56.7)	13 (43.3)	10 (55.6)	8 (44.4)	
> 40	11 (55.0)	9 (45.0)	6 (50.0)	6 (50.0)	
TB (μmol/L)					0.180
≤ 19	21 (56.8)	16 (43.2)	14 (53.8)	12 (46.2)	
> 19	7 (53.8)	6 (46.2)	2 (50.0)	2 (50.0)	
CB (μmol/L)					0.614
≤ 6.8	20 (58.8)	14 (41.2)	12 (54.5)	10 (45.5)	
> 6.8	8 (50.0)	8 (50.0)	4 (50.0)	4 (50.0)	
ALB (g/L)					0.698
≤ 40	23 (62.2)	14 (37.8)	11 (52.4)	10 (47.6)	
> 40	5 (38.5)	8 (61.5)	5 (55.6)	4 (44.4)	
PLT					
≤ 100 × 10^9/L	6 (54.5)	5 (45.5)			
> 100 × 10^9/L	22 (56.4)	17 (43.6)	16 (53.3)	14 (46.7)	
INR					0.093
≤ 1.15	18 (54.5)	15 (45.5)	15 (60.0)	10 (40.0)	
> 1.15	10 (58.8)	7 (41.2)	1 (20.0)	4 (80.0)	
PT (s)					0.407
≤ 13	19 (55.9)	15 (44.1)	14 (60.9)	9 (39.1)	
> 13	9 (56.3)	7 (43.8)	2 (28.6)	5 (71.4)	

Table 1 (continued)

Variables	Training cohort ($n = 50$)		Validation cohort ($n = 30$)		P
	MVI−	MVI+	MVI−	MVI+	
Scr (μmol/L)					
≤ 133	28 (56.0)	22 (44.0)	16 (53.3)	14 (46.7)	
> 133					
AFP (ng/ml)					0.064
≤ 200	18 (56.3)	14 (43.8)	14 (56.0)	11 (44.0)	
> 200	10 (55.6)	8 (44.4)	2 (40.0)	3 (60.0)	
SUVmax	4.58 ± 4.25	7.66 ± 6.00	4.89 ± 3.20	8.29 ± 4.48	0.629
TLR	1.98 ± 1.04	3.46 ± 2.56	2.27 ± 1.71	3.48 ± 1.79	0.653

HBV, hepatitis B virus; *ALT*, alanine transaminase; *AST*, glutamic-oxal (o) acetic transaminase; *TB*, serum total bilirubin; *CB*, conjugated bilirubin; *ALB*, albumin; *PLT*, platelet count; *INR*, international normalized ratio; *PT*, prothrombin time; *Scr*, serum creatinine; *AFP*, serum α-fetoprotein

vein, or a large capsular vessel of the surrounding hepatic tissue lined by the endothelium that was visible only on microscopy [20, 21].

PET/CT imaging

[18F]FDG was synthesized using the Tracer lab F_XFN synthesis system (TRACERlab F_XFDG; GE Healthcare, USA). PET/CT scan was performed using a BiographmCTx scanner (Discovery ST 8, GE Healthcare, WI, USA, and Siemens, Germany). Patients were instructed to fast for at least 4 h. The blood glucose levels of patients ranged from 3.6 to 6.1 mmol/L before [18F]FDG injection. Approximately 60 min after the intravenous injection of 3.70–5.55 MBq/kg of [18F]FDG, PET/CT data were acquired according to the guidelines for tumor imaging with [18F]FDG PET/CT 1.0. Then, PET images were converted into SUV units by normalizing the activity concentration to the dosage of [18F]FDG injected and patient body weight after decay correction.

VOI drawing and image analyzing

[18F]FDG PET/CT images were exported to the Lifex software (version 5.10) [22]. PET/CT images were analyzed by an experienced nuclear medicine physician with more than 20 years of experience in PET/CT diagnosis (XL Wang). Areas with abnormal uptake of [18F]FDG on PET and/or abnormal density on CT were defined as lesions. On the PET image, an ellipse iso-contour was drawn covering the lesion, and the volume of interest (VOI) in 3D was obtained semi-automatedly with an iso-contour threshold of 30% maximum. If the PET and CT images matched well, the VOI of PET was then copied to CT images to obtain the VOI on CT. If the lesion had a low uptake of [18F]FDG, the VOI was calculated on CT images and was then copied to PET to obtain the VOI on PET. On the CT images, the regions of interest (ROIs) were

drawn section by section to measure the VOI. Enhanced contrast CT and MRI were sometimes used to help determine the VOI. VOIs for PET and CT were drawn respectively in case of the mismatching of lesions border on PET and CT. The texture features were then automatically extracted from the PET and CT images. Tumor FDG avidity was measured by tumor-to-normal liver standardized uptake value ratio (TLR) calculated with the following equation: TLR = maximum SUV of the tumor/mean SUV of the normal liver.

Then, the images were resampled to $1 \times 1 \times 1$ mm^3 voxels by three-dimensional Lagrangian polygon interpolation. On the CT images, Hounsfield units were then resampled into 400 discrete values (called bins) with absolute discretization from − 1000 to 1000 Hounsfield units, leading to a fixed bin size of 5.0 Hounsfield units. Four gray-level matrices were calculated in three dimensions, giving 49 radiomics features (including first-order and second-order features and volumes) for each of the CT-tumor VOIs. On the PET images, SUV units were resampled into 64 discrete values with absolute discretization from 0 to 30 SUV units, leading to a fixed bin size of 0.476 SUV units. Four gray-level matrices were calculated in three dimensions, giving 52 radiomics features for each of the PET-tumor VOIs. Values of extracted radiomics features were normalized using the Z-transform method [23]. All the texture features were summarized and defined in detail in the Supplemental Materials.

Feature selection and radiomics signature construction

The least absolute shrinkage and selection operator (LASSO) method was used to select the most useful features from the training cohort for prediction. A radiomics score (Rad-score) was calculated for each patient via a linear combination of selected features that were weighted by their respective coefficients.

Development of individualized prediction models

Univariable and multivariable logistic regression analyses or Cox regression analyses were used to analyze the value of clinical candidate predictors. Radiomics signature was applied to develop a diagnostic model for the prediction of MVI status and DFS. Backward stepwise selection was applied using the likelihood ratio test with Akaike's information criterion as the stopping rule. Patients were classified into the high-risk group and the low-risk group using the X-tile analyses for the radiomics signature [24]. To provide the clinician with a quantitative tool to predict MVI and DFS, a radiomics nomogram was built based on multivariable analysis.

Assessment of nomogram performance

Calibration curves were plotted to assess the calibration of the radiomics nomograms and were accompanied by Hosmer-Lemeshow tests (a significant test statistic implies that the model does not calibrate perfectly). To quantify the discrimination performance of the radiomics nomogram, area under the curve (AUC) or Harrell's C-index was calculated.

Validation of the radiomics nomogram

The radiomics nomogram was subjected to bootstrapping validation (10 bootstrap resamples) to draw the time-dependent C-index curves in the training cohort. Then, the model created in the training cohort was applied to all patients in the validation cohort and the performance of the internally validated nomogram was tested in the validation cohort. The AUC/C-index and calibration curves were derived based on the regression analyses.

Clinical utility of the radiomics nomogram

To estimate the clinical utility of the nomograms, decision curve analyses (DCA) were performed by calculating the net benefits for a range of threshold probabilities in the training cohort and validation cohort.

Statistical analysis

All statistical tests were performed using SPSS 24.0 and R statistical software (version 4.0.2). The differences in age, sex, BCLC stage, mean follow-up time, and other related clinical information between the training and validation cohort were assessed using independent sample t test, χ^2 test, or Mann-Whitney U test, where appropriate.

The selected features after Z-transformation and the clinical features were revealed by a heatmap using an online tool called Morpheus (https://software.broadinstitute.org/morpheus). Univariate and multivariate regression analyses were used to evaluate the prediction value by SPSS 24. To predict MVI status, binary logistic regression analyses were used. To predict DFS, we used Cox regression analyses. A two-sided $P < 0.05$ was considered significant.

We used the "glmnet" package to perform the LASSO regression analysis. Nomogram construction and calibration plots were performed using the "rms" and "pec" packages. Bootstrapping validation of the radiomics nomogram was accomplished using the "hdnom" package. Comparison of two time-dependent AUCs was performed using the "time ROC" package. The survival curves were obtained by the "survminer" package. DCA was performed using the "rmda" and "ggDCA" package.

Results

Clinical characteristics

The study flowchart for predicting MVI and DFS via analysis of PET and CT texture features and clinical risk factors is presented in Fig. 1. Patient characteristics in the training cohort and validation cohort are given in Table 1. Of the 80 patients with BCLC0-A HCC, 45.0% (36/80) had the tumors with MVI (MVI+) and 55.0% (44/80) patients had the tumors without MVI (MVI−). MVI positivity was detected in 44.0% (22/50) of tumors in the training cohort, similar to 46.7% (14/30) seen in the validation cohort ($P = 0.816$). Follow-up data showed that 50.0% of patients in the training cohort experienced tumor relapse, which was not significantly different from the 46.7% seen in the validation cohort ($P = 0.773$). Univariate analyses revealed that there was also no significant difference in patients' clinical and histological characteristics between training and validation cohort ($P > 0.05$, Table 1). The above information indicated that the patients in the training and validation cohort had a balanced distribution of survival and baseline clinical-pathologic characteristics.

Development of the predictive models for MVI status

Univariable analyses were used to determine the relationship between clinical and histopathological features and imaging indicators with MVI status (Table 2). According to the results of the univariable analysis, none of the clinical factors was found to be closely related with MVI status (Table 2, $P > 0.05$ for all clinical features), neither the histopathological features, including BCLC stage, tumor differentiation and Child-Pugh classification (Table 2, $P > 0.05$). For the three conventional imaging indicators, the diameter was also not related to MVI status (Table 2, $P > 0.05$); however, close associations were observed between SUV_{max} and TLR with MVI in training cohort ($P < 0.05$).
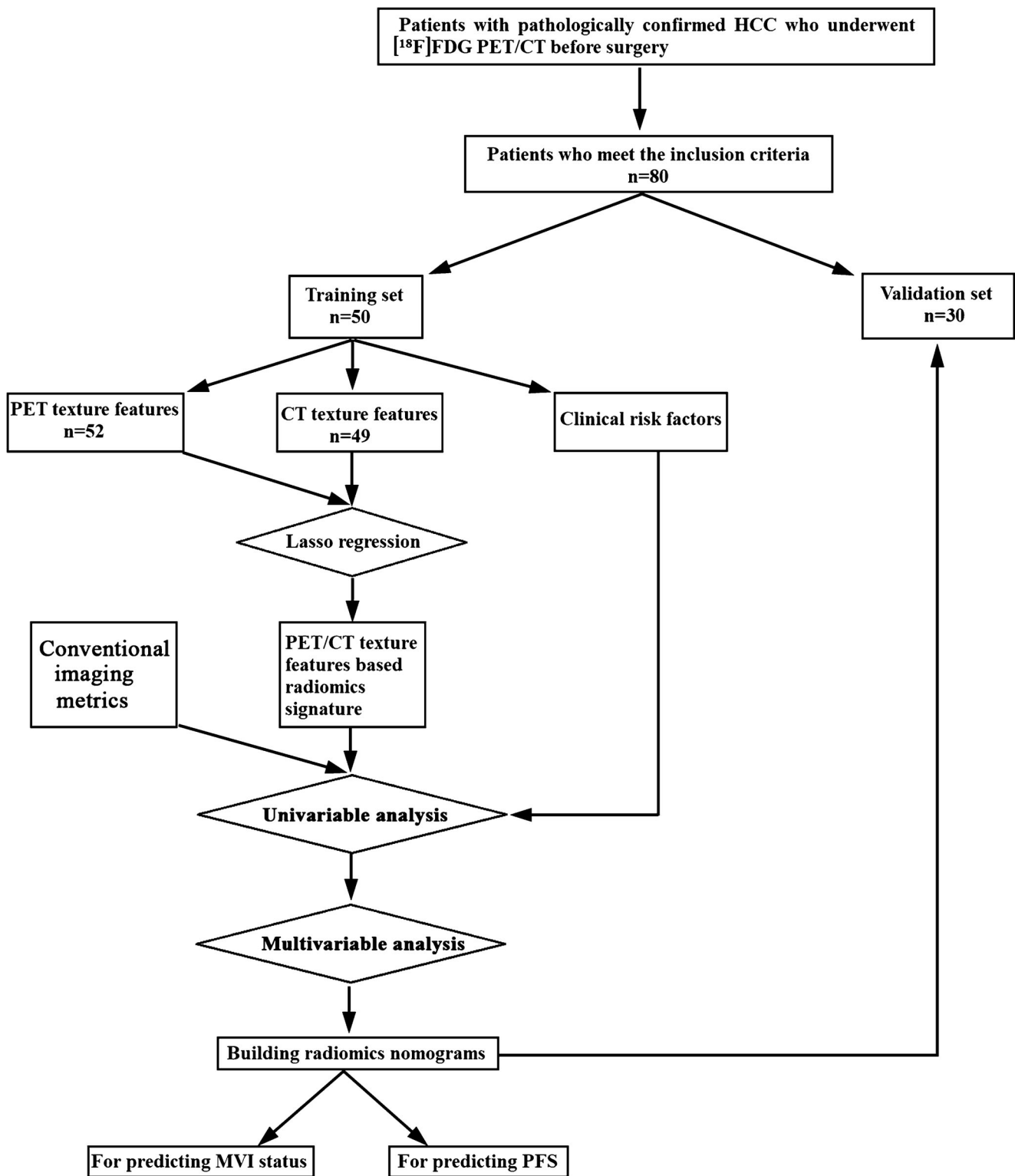
Fig. 1 Study flowchart for predicting MVI and DFS by analyzing PET and CT texture features and clinical risk factors in training and validation set

Potential radiomics features were selected to establish PET/CT model (M-PET/CT model) for predicting MVI status using the LASSO regression on the basis of 50 patients in the training cohort. LASSO analysis revealed that five PET texture features (HISTO_Entropy_log2, HISTO_Energy, GLCM_Contrast, NGLDM_Busyness, GLZLM_ZP), and six CT texture features (CONVENTIONAL_HUmax, CONVENTIONAL_HUQ3, HISTO_Kurtosis, HISTO_ExcessKurtosis, NGLDM_Coarseness, GLZLM_ZLNU), were most useful for predicting the MVI status. From the above-selected

Table 2 Univariate cox regression analyses for MVI in the training cohort

Variables	B	SE	Wald	Sig.	Exp (B)	95.0% CI for Exp (B)	
						Lower	Upper
Sex	− 0.924	1.192	0.601	0.438	0.397	0.038	4.105
Age	0.272	0.585	0.216	0.642	1.313	0.417	4.131
Diameter	0.665	0.345	3.703	0.054	1.944	0.988	3.826
PT	− 0.015	0.611	0.001	0.981	0.985	0.297	3.263
INR	− 0.174	0.604	0.083	0.773	0.840	0.257	2.745
PLT	− 0.076	0.686	0.012	0.912	0.927	0.242	3.559
TB	0.118	0.648	0.033	0.856	1.125	0.316	4.005
CB	0.357	0.609	0.343	0.558	1.429	0.433	4.717
ALB	0.966	0.663	2.123	0.145	2.629	0.716	9.645
AST	0.068	0.581	0.014	0.907	1.070	0.342	3.342
ALT	0.318	0.664	0.230	0.632	1.375	0.374	5.055
HBsag	− 1.061	0.919	1.333	0.248	0.346	0.057	2.095
AFP	0.028	0.593	0.002	0.962	1.029	0.322	3.290
Child-pugh	− 0.054	0.823	0.004	0.948	0.947	0.189	4.756
BCLC	0.205	0.719	0.081	0.776	1.227	0.300	5.028
Cirrhosis	− 0.154	0.620	0.062	0.804	0.857	0.254	2.890
Differentiation	0.320	0.793	0.162	0.687	1.377	0.291	6.519
SUVmax	2.750	0.709	15.054	0.000^*	15.640	3.899	62.735
TLR	2.134	0.729	8.559	0.003^*	8.444	2.022	35.262
M-R-score	2.158	0.660	10.694	0.001^*	8.654	2.374	31.547

* These variables were statistically significant for predicting MVI status in the univariate analyses

radiomics features, Rad-score for PET/CT (M-R-score) was calculated. Calculation formula for the Rad-score based on radiomics features was presented in the Supplemental Data. As a result, M-R-score was proved to be statistically associated with MVI ($P = 0.001$, Table 2). The heatmap, which was used to visualize the rough association of clinical features and M-R-score with MVI status, is provided in Figs. S1 and S2 in the Supplemental Data. From the results of univariable analyses, SUV_{max}, TLR and M-R-score were then brought into the multivariable logistic analysis, which finally demonstrated that only M-R-score was the independent predictor for predicting the MVI status ($P = 0.001$, Table 4). Only the M-R-score was used to build predictive model (named M-PET/CT model) for MVI status.

Assessment and validation of prediction models for MVI status

In order to identify the prediction performance, the ROC curves for the M-PET/CT model in the training and validation cohort were drawn (Fig. 2a, b). The AUC of M-PET/CT model in the training cohort was found to be 0.891(95% CI: 0.799–0.984) (Fig. 2a). The optimum cut-off of M-R-score generated by the AUC was 0.07. In this condition, the predicting sensitivity was 0.682 and the specificity was 0.964. The AUC of the M-PET/CT model in the validation

cohort was 0.692 (95% CI: 0.497–0.887). The Hosmer and Lemeshow tests showed good fits not only in the training cohort ($P = 0.796$) but also in validation cohort ($P = 0.874$). The calibration curve of the M-PET/CT model for predicting MVI demonstrated good agreement between prediction and observation in training cohort (Fig. 2c). However, the unfavorable calibration of the M-PET/CT model was observed in validation cohort (Fig. 2d).

Clinical use

The decision curve analysis for the M-PET/CT model in the training and validation cohort is presented in Fig. 2e, f. The decision curve showed that if the threshold probability of a patient or doctor is > 10%, using the M-PET/CT model to predict MVI adds more benefit than either the treat-all-patients scheme or the treat-none scheme.

Feature selection and radiomics nomograms building for predicting DFS

According to the results of follow-up, a total of 39 patients, including 25 patients (50%) in the training cohort and 14 patients (46.7%) in the validation cohort, had the tumor relapse.
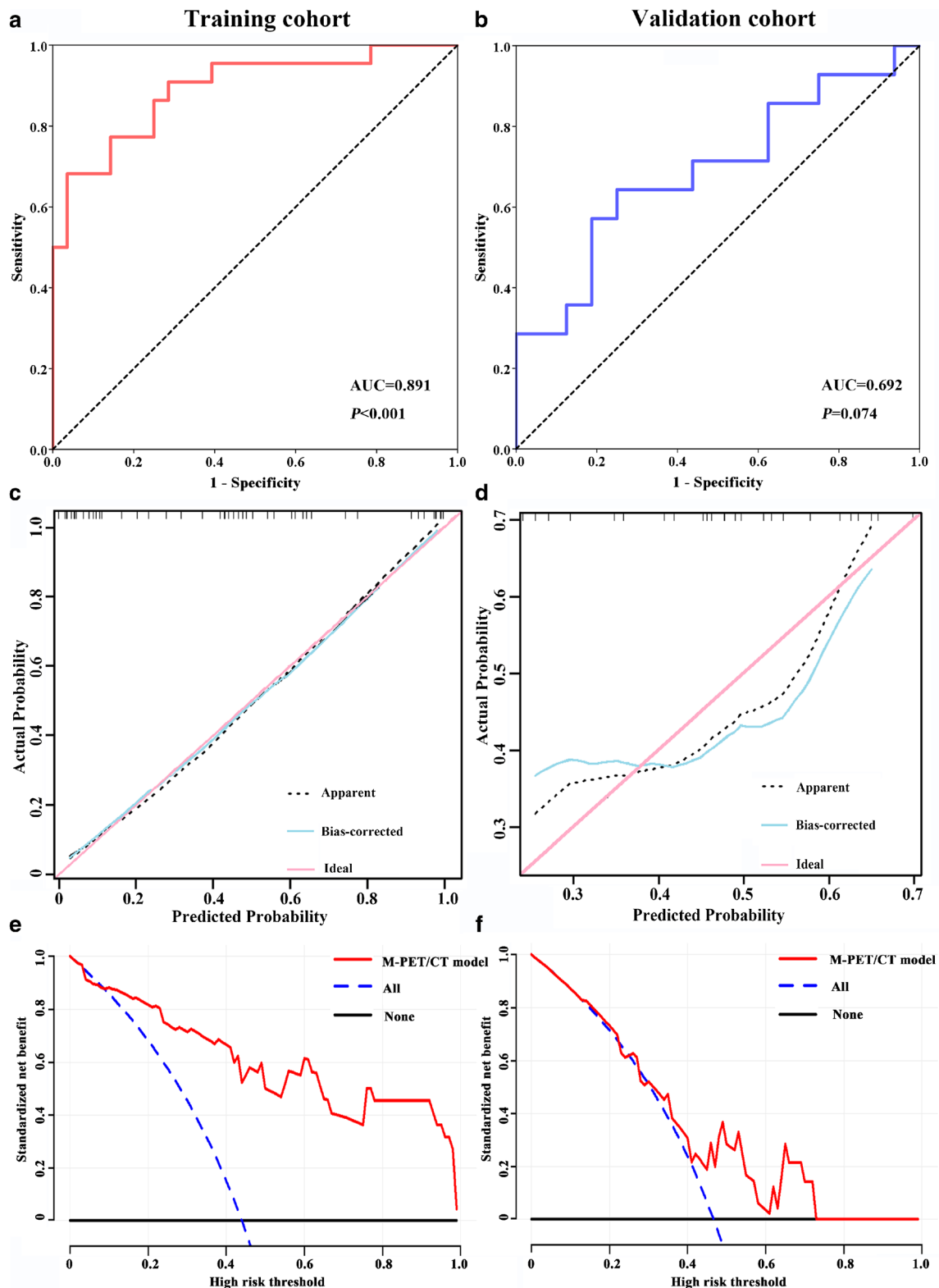
Fig. 2 a, **b** ROC curve for the M-PET/CT model in the training (**a**) and validation (**b**) cohorts. **c**, **d** Calibration curves of the M-PET/CT model for MVI prediction in the training (**c**) and validation (**d**) cohorts. **e**, **f** Decision curve analysis for M-PET/CT model in training cohort (**e**) and validation cohort (**f**)

The LASSO regression analyses revealed that three PET texture features (HISTO_Energy_Uniformity, GLCM_Contrast_Variance, NGLDM_Coarseness) and four

CT texture features (CONVENTIONAL_HUQ2, CT_HISTO_Kurtosis, CT_HISTO_ExcessKurtosis, CT_NGLDM_Busyness) were most useful for predicting

DFS. PET/CT Rad-score (D-R-score) was then calculated based on the above texture features. The formula of Rad-score for predicting DFS was listed in the Supplemental Materials. The D-R-score optimum cut-off point generated by the X-tile analysis was identified at 0.5. Accordingly, patients were classified into the low-risk group (Rad-score < 0.5) and the high-risk group (Rad-score ≥ 0.5). The relationship between DFS and the clinical factors and histopathologic and imaging indicators were investigated. Among them, 6 variables including 4 clinical variables (INR, CB, TB and MVI) and 2 conventional PET imaging metrics (SUV_{max} and TLR) were identified to be closely related with DFS by univariate analysis ($P < 0.05$ for all) (Table 3 and Table 4, Fig. 3). The D-R-score was observed to be significantly associated with DFS ($P < 0.001$) (Table 3, Fig. 4). In the training cohort, Kaplan-Meier analysis showed the D-Rad-score was significantly correlated with tumor relapse and the patients with higher Rad-scores had a significantly higher incidence of tumor recurrence ($P < 0.05$, Fig. 4a). 13 (34.2%) patients were confirmed to have tumor relapses in the low-risk group; 12 (100%) patients in the high-risk group were confirmed to have tumor relapse (mean DFS, 40.82vs9.08 months, $P < 0.0001$). A similar result was also observed in the D-R-score in the validation cohort (Fig. 4b). Further multivariate analysis revealed that the INR, TB and D-R-score were statistically significant for predicting DFS. These three features were applied to develop the predictive model for DFS, which was named the D-PET/CT model. Meanwhile, a clinical model was also built after multivariate analysis of the clinical variables in the training cohort. The clinical model was integrated by the INR, TB, and MVI status. To provide the clinician with a quantitative method to predict patients' probability of 1-, 2- and 3-year DFS, the nomograms of the D-PET/CT model and clinical model were developed (Fig. 5a–d).

Assessment and validation of prediction models for DFS

The C-indices of the D-PET/CT model and clinical model in the training cohort were 0.831(95% CI, 0.761 to 0.900) and 0.776(95% CI, 0.689 to 0.862), respectively. The C-index of the D-PET/CT model was superior to that of clinical model in the training cohort ($P = 0.04$). Using time-dependent receiver operating characteristic curve analysis, we found that the D-PET/CT model had higher predictive power for HCC recurrence than the clinical model at various time points in the training cohort (Fig. 5c, d). The C-indices of the two models for predicting DFS in the validation cohort were 0.640 (95% CI, 0.487 to 0.793) and 0.692 (95% CI, 0.552 to 0.832), respectively.

The calibration curves for predicting the probability of tumor recurrence at 1, 2, or 3 years after surgery of each model after 1000 times of bootstraps are shown in Fig. 5e–h. The calibration curves showed similarly good agreement between the estimation and actual observation in the training cohort. Correlation matrix for all the eligible features in the training cohort is shown in the Fig. S3.

Clinical use

The decision curve analyses for the D-PET/CT model and clinical model are presented in Fig. 6. Decision curve analyses showed that the D-PET/CT radiomics nomogram had a higher overall net benefit than the clinical-pathologic nomogram across most of the range of risk threshold (Fig. 6a). Decision curve analyses in the validation cohort were a little unsatisfactory but kept a similar trend with that in the training cohort (Fig. 6b).

Discussion

The prediction of MVI and the tumor recurrence in patients with very early and early HCC (BCLC stage 0-A) are important for establishing a precise therapeutic strategy. Despite improvements in diagnostic and therapeutic modalities, the recurrence rate after treatment for HCC remains high [25]. Approximately half of the patients in our study developed tumor relapse. MVI is an important factor related to the recurrence of HCC. Preoperatively predicting MVI and DFS in patients with very early or early HCC (BCLC stage 0 or A) is important for establishing a personalized therapeutic strategy and helps to select a more aggressive treatment for those with high-risk factors in order to reduce the post-operation recurrence. In this study, we found that the radiomics signature of preoperative [18F]FDG PET/CT from patients with very-early- and early-stage HCC was an independent predictor for MVI status, while the clinical features were not. Meanwhile, we also demonstrated the role of the radiomics of preoperative [18F]FDG PET/CT in predicting DFS. Based on the above findings, we developed and validated a radiomics feature-based [18F]FDG PET/CT nomogram and a clinical nomogram for predicting DFS. Our data revealed that the D-PET/CT nomogram successfully stratified patients into high-risk and low-risk groups, with significant differences in DFS within 3 years. The D-PET/CT model performed better than the clinical-pathologic nomogram, indicating the incremental value of the D-PET/CT radiomics signature for individualized DFS in patients with very-early- and early-stage HCC.

Some studies reported that preoperative metabolic biomarkers of the HCCs, such as SUV_{max} and TLR, are independent predictors of MVI [26–28]. In agreement with their results, univariate analysis in our study also found that SUV_{max} and TLR were closely associated with MVI ($P < 0.05$), as higher SUV_{max} and TLR showed higher frequencies of

Table 3 Univariate cox regression analyses for disease-free survival in the training cohort

Variables	B	SE	Wald	Sig.	Exp (B)	95.0% CI for Exp (B)	
						Lower	Upper
Sex	0.312	0.616	0.257	0.612	1.367	0.408	4.575
Age	0.268	0.418	0.411	0.521	1.307	0.576	2.964
Diameter	0.359	0.239	2.248	0.134	1.432	0.896	2.289
PT	0.746	0.404	3.403	0.065	2.109	0.954	4.659
INR	0.885	0.402	4.836	*0.028*[*]	2.422	1.101	5.330
PLT	−0.732	0.420	3.034	0.082	0.481	0.211	1.096
CB	0.899	0.402	5.000	*0.025*[*]	2.457	1.117	5.405
TB	1.181	0.414	8.130	*0.004*[*]	3.256	1.446	7.332
ALB	0.343	0.430	0.635	0.426	1.409	0.607	3.271
AST	0.640	0.402	2.544	0.111	1.897	0.864	4.168
ALT	0.717	0.432	2.759	0.097	2.048	0.879	4.773
HBsag	0.656	0.739	0.788	0.375	1.926	0.453	8.194
AFP	0.447	0.403	1.227	0.268	1.563	0.709	3.445
Child-pugh	0.527	0.507	1.083	0.298	1.694	0.628	4.572
BCLC	0.396	0.547	0.525	0.469	1.486	0.509	4.340
Cirrhosis	−0.069	0.430	0.026	0.873	0.934	0.402	2.168
Differentiation	−0.661	0.469	1.984	0.159	0.516	0.206	1.295
MVI	1.256	0.421	8.897	*0.003*[*]	3.512	1.538	8.016
SUVmax	0.107	0.033	10.470	*0.001*[*]	1.113	1.043	1.188
TLR	0.262	0.087	9.147	*0.002*[*]	1.300	1.097	1.541
D-R-score	1.045	0.248	17.762	*0.000*[*]	2.842	1.749	4.621

[*] These variables were statistically significant for predicting DFS in the univariate cox regression analyses

Table 4 Univariate and multivariable Cox regression analysis of predictors in three predicting Models for MVI and DFS in the training cohort

Variable	Univariable			Multivariable		
	HR	95% CI	*P*	HR	95% CI	*P*
Predict MVI						
M-PET/CT model						
SUVmax	15.640	3.899–62.735	0.000			
TLR	8.444	2.022–35.262	0.003			
M-R-score	8.654	2.374–31.547	0.001	8.654	2.374–31.547	0.001
Predict DFS						
D-PET/CT model						
INR	2.422	1.101–5.330	0.028	3.786	1.485–9.653	0.005
CB	2.457	1.117–5.405	0.025			
TB	3.256	1.446–7.332	0.004	4.124	1.696–10.028	0.002
MVI	3.512	1.538–8.016	0.003			
SUV$_{max}$	1.113	1.043–1.188	0.001			
TLR	1.300	1.097–1.541	0.002			
D-R-score	2.842	1.749–4.621	0.000	3.295	1.651–6.574	0.001
Clinical model						
INR	2.422	1.101–5.330	0.028	2.723	1.183–6.267	0.018
CB	2.457	1.117–5.405	0.025			
TB	3.256	1.446–7.332	0.004	3.441	1.458–8.122	0.005
MVI	3.512	1.538–8.016	0.003	4.973	2.075–11.917	0.0003
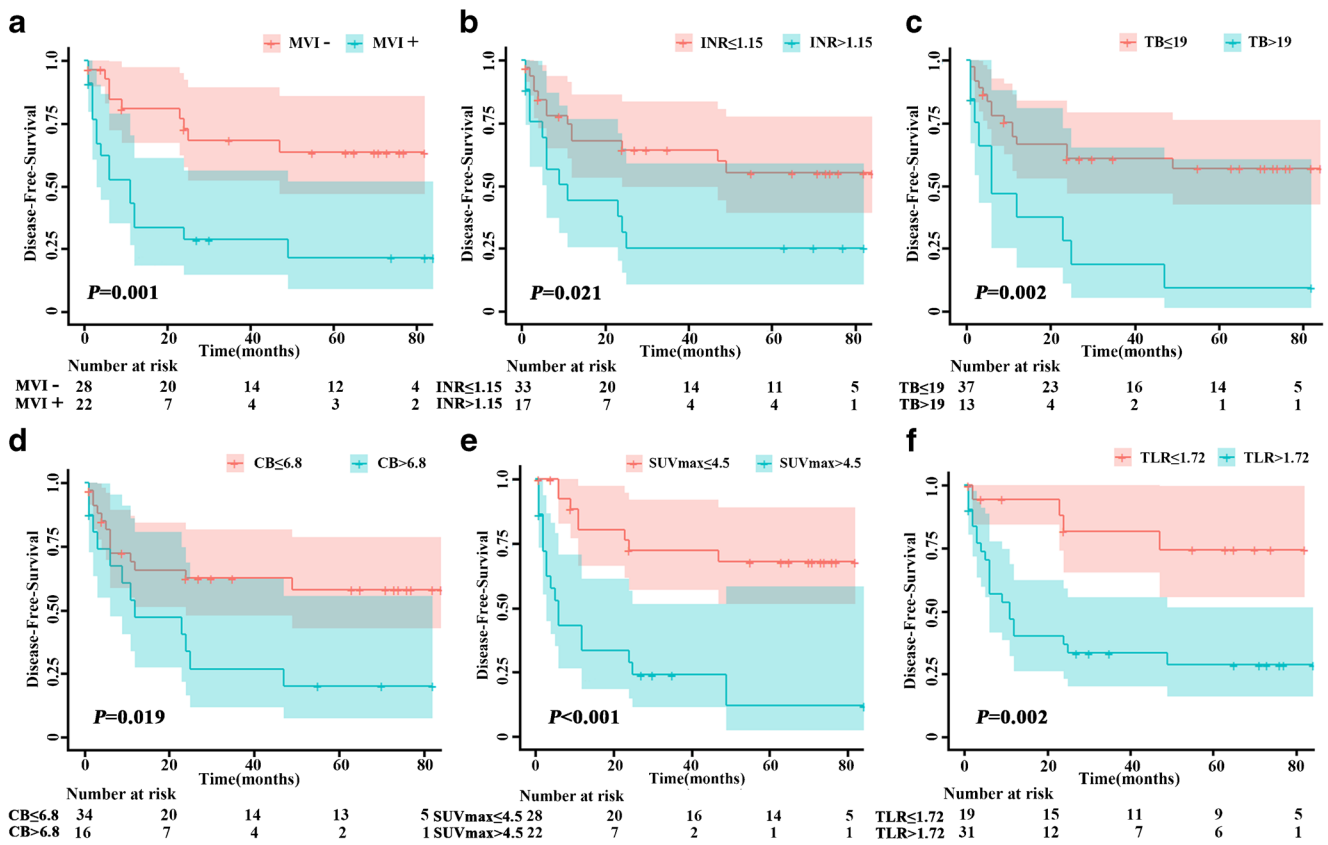
Fig. 3 Kaplan-Meier analyses of the 6 selected features for patients in the training cohort

microvascular infiltration than the lower glucose metabolism. However, all of the clinical features were not significantly associated with MVI ($P > 0.05$), which is different from reports by Xu and Seung et al. [18, 21]. In their studies, some clinical features such as clinical stage, AST, and AFP are important predictors of MVI [21, 29]. This difference is likely due to the difference in study object, as their studies included advanced liver cancer, whereas we only enrolled patients with very-early- and early-stage HCC. In our study, most patients had the low grade of HCC and preserved liver function, which
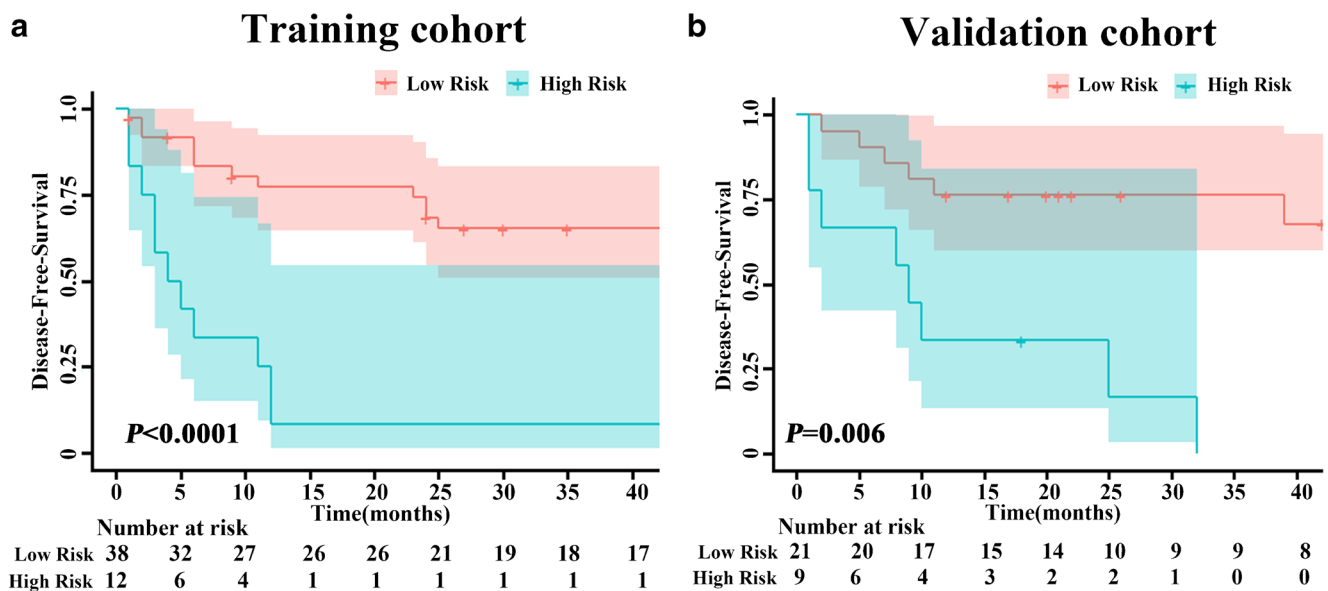
Fig. 4 **a**, **b** Survival of patients stratified by the risk classification according to D-PET/CT radiomics signature for patients in the training (**a**) and validation (**b**) cohorts
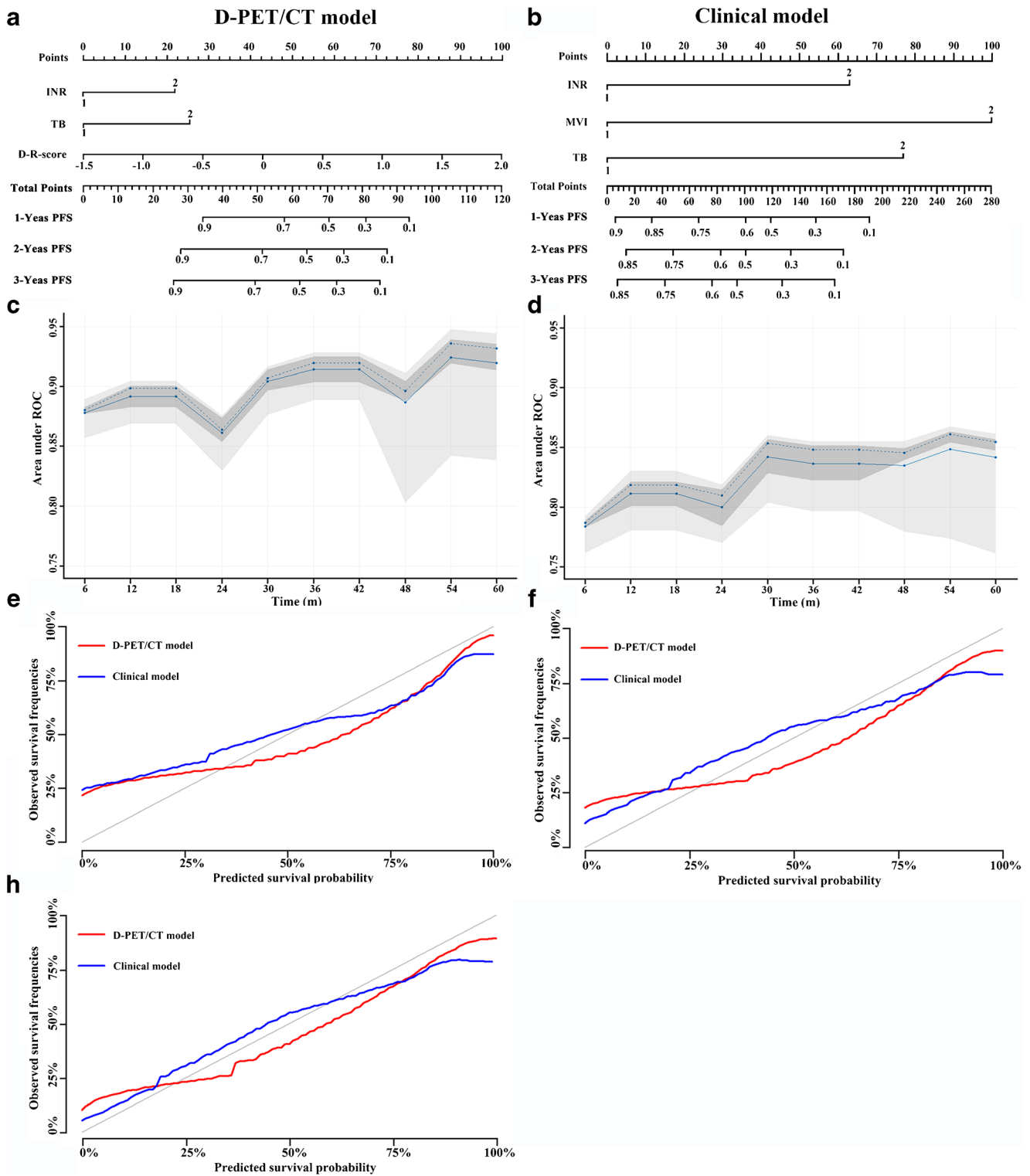
Fig. 5 **a**, **b** Radiomics nomogram of the D-PET/CT model and clinical model for predicting DFS. **c**, **d** Time-dependent area under ROC curve of the D-PET/CT model and clinical model for DFS prediction. **e–h** Calibration curves of D-PET/CT model and clinical model for DFS prediction in the training cohort at the 1-year (**e**), 2-year (**f**), and 3-year (**h**) time points

might be one of the reasons that the clinical features were not significant predictors for MVI status. However, multivariate analysis showed that only the radiomics signature (M-R-score) was an independent predictor for MVI status in very-early- and early-stage HCC ($P < 0.05$). Our study revealed that the radiomics signature of $[^{18}F]$FDG PET/CT was a stable predictor of MVI status with relatively high AUCs and calibrations. Ultrasound, contrast-enhanced CT and the gadoxetic

acid–enhanced MRI based models had been used for predicting MVI status. The gadoxetic acid–enhanced MR model had the highest AUC (0.936; 95% CI 0.895–0.976) for predicting MVI status [30], followed by the contrast-enhanced CT model, both of which worked better than the ultrasound-based model [12]. The blood supply could be assessed via contrast-enhanced CT or MR, which may contribute to the high AUCs for prediction. When compared with other reported models, our study demonstrated that the M-PET/CT model (0.891, 95% CI: 0.799–0.984) exhibited similar performance with the contrast-enhanced CT model (0.909, 95% CI, 0.869–0.928). The CT component of the PET/CT had a relatively poor performance in assessing MVI due to its specific image acquisition (low dose without contrast enhancement). The performance improvement of the M-PET/CT model was likely due to the addition of the PET component.

Resection for early-stage HCCs is still plagued by a high recurrence rate, and approximately half of the patients in our study developed tumor relapse, which was in agreement with the results of previous studies [31, 32]. In this study, we revealed that the radiomics signature of [^{18}F]FDG PET/CT was a stable predictor for MVI. However, the relationship between MVI, PET/CT based radiomics, and early tumor recurrence in very-early- and early-stage HCC remains unclear. Although the Barcelona Clinic Liver Cancer system is crucial for assessing the prognosis and establishing a treatment strategy, this staging system performs poorly in predicting tumor recurrence after hepatic resection or orthotopic liver transplantation for HCC [29]. In this study, Kaplan-Meier analysis revealed

that there was no significant difference in the DFS distribution between BCLC 0 stage and the group of BCLC A stage ($P = 0.269$, Fig. S4a). Within BCLC A, the radiomics signature successfully identified high-risk patients with poor survival outcomes, for whom more intensified treatment was needed (Fig. S4b). Unfortunately, the radiomics signature failed to discriminate subgroups within stage BCLC 0 ($n = 14$), which may be largely attributed to the limited size of the study population. Unlike prior prognostic investigations that mainly analyzed patients at all stages of the disease, our current study focused exclusively on patients with very-early- and early-stage disease. Therefore, we sought to improve the predictive ability for prognosis of very early and early HCC by developing a novel method for categorizing patients into low- and high-risk groups for early tumor recurrence. To our knowledge, the association between radiomics features of PET/CT images and DFS of HCC patients has not been evaluated previously.

Radiomics refers to the comprehensive quantification of tumor phenotypes by applying a large number of quantitative imaging features, which may reflect changes in human tissues at the cellular and genetic levels, and provides more detailed information on tumor biology and microenvironment that are complementary to visual features [33, 34]. In this study, the extraction of advanced PET imaging features allowed us to assess intratumor heterogeneity quantitatively on the glucose metabolism scale. Cox regression analysis showed that the radiomics signature was an independent prognostic factor for DFS in very-early- and early-stage hepatocellular carcinoma, even after adjustment for the same stage (Fig. S4b). In order to
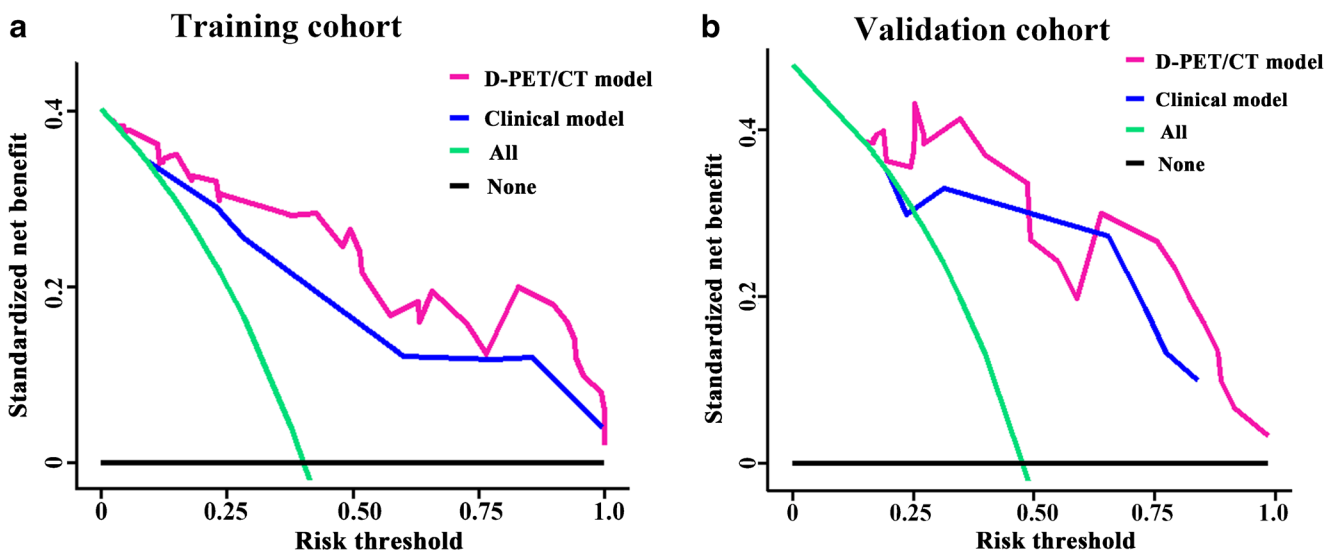
Fig. 6 Decision curve analysis for each model in training cohort (**a**) and validation cohort (**b**). The *y*-axis measures the net benefit. The net benefit was calculated by summing the benefits (true positive results) and subtracting the harms (false-positive results), weighting the latter by a factor related to the relative harm of an undetected cancer compared with the harm of unnecessary treatment. The radiomics model had the highest net benefit compared with both clinical model and simple strategies such as follow-up of all patients (green line) or no patients (horizontal black line) across the full range of threshold probabilities at which a patient would choose to undergo imaging follow-up in the training cohort

use it for clinical practice, we established a radiomic-based prediction model and a clinical model for predicting HCC recurrence. We found that the prognostic performance of the radiomic-based model (D-PET/CT model) was superior to that of the clinical model in the training cohort ($P < 0.05$). The D-PET/CT model had a higher capability for risk assessment of early recurrence after radical resection of very early and early HCC and yielded the best discriminatory capacity (Fig. 5c, d). The metabolic signature of [^{18}F]FDG PET/CT, a multi-parametric approach using fully integrated [^{18}F]FDG PET/CT, successfully stratified those patients into high-risk and low-risk groups with significant differences in DFS within 3 years. Patients at high risk for recurrence are potential candidates for more intensive surveillance and adjuvant therapy after curative surgery. Study findings have supported the prognostic value of the signature and allowing clinicians to potentially identify candidates for systemic approaches with greater effectiveness to improve treatment outcomes. Moreover, incorporation of D-PET/CT radiomics signatures into a clinical model can add prognostic information to better identify patients that may have different outcomes, and the radiomics nomogram is a good witness. The decision curve analysis demonstrated that the D-PET/CT radiomics nomogram was superior to the clinical-pathologic nomogram across most of the range of reasonable threshold probabilities, indicating that the D-PET/CT radiomics signature added incremental value to other clinical-pathologic risk factors for individualized DFS estimation.

Microvascular invasion is a well-known independent prognostic factor associated with more advanced tumor stage, tumor progression, and poorer clinical outcomes. In this study, the microvascular invasion was a high-risk factor associated with DFS (Fig. 3a). However, further analysis revealed that the radiomics signature is the independent prognostic factor, but not MVI (Table 4). As demonstrated in the current study, radiomics feature-based [^{18}F]FDG PET/CT imaging signature by applying a large number of quantitative image features could be suggestive of survival outcomes, which may reflect changes of human tissues at the cellular and genetic levels and provide different information from MVI and thus is associated with patient prognosis. Except for radiomics signature, TB and INR were also significantly associated with DFS even in very early and early HCC and were risk factors for DFS prediction models (Fig. 3b, c), similar to the results of other studies that liver function is another independent prognosticator of tumor recurrence [35–37]. Previous studies have explored the relationship between SUV$_{max}$ and HCC outcomes. HCCs with increased [^{18}F]FDG uptake showed molecular features of more aggressive biologic properties than those with a low [^{18}F]FDG uptake [14]. The findings of this study support the above hypothesis that patients with a high SUV$_{max}$ and TLR demonstrated a worse overall survival (Fig. 3e, f).

Our study has some limitations. First is the small sample size and the retrospective evaluation of data. The relationship between the clinicopathological parameters, MVI, and prognosis could have been influenced by the small sample size. To overcome these limitations, we are aiming at validating the model in prospective multi-center clinical trials. Finally, whether adjuvant therapy can provide a better survival benefit to patients classified as high Rad-score based on [^{18}F]FDG PET/CT nomogram should be assessed in the future.

Conclusion

This study provided [^{18}F]FDG predictive model that incorporated both the radiomics signature of [^{18}F]FDG PET/CT and clinical risk factors. The radiomics signature can be conveniently used to facilitate the preoperative individualized prediction for MVI status and DFS in patients with very-early- and early-stage HCC. The radiomics signature of [^{18}F]FDG PET/CT effectively predicted MVI status. Incorporating D-PET/CT radiomics into a nomogram along with other clinical-pathologic risk factors to estimate the disease-free survival for very early and early HCC was more accurate than the clinical-pathologic nomogram. Our predictive models are potential, noninvasive, and effective complements to clinical practice. The radiomics analysis could renew the application of [^{18}F]FDG for management of HCC.

Data availability All data were transparent. The data used in the current study are available from the corresponding authors on reasonable request.

Compliance with ethical standards

Conflict of interest The authors declare that they have no conflict of interest.

Ethics approval Ethical approval was waived by the local Ethics Committee of Guangzhou Medical University and Southern Medical University in view of the retrospective nature of the study.

Consent to participate Due to the retrospective nature of the study, informed consent was not obtained in the study.

Code availability The code used in the current study is available from the corresponding authors on reasonable request.

References

1. Marrero JA, Welling T. Modern diagnosis and management of hepatocellular carcinoma. Clin Liver Dis. 2009;13:233–47. https://doi.org/10.1016/j.cld.2009.02.007.

2. Forner A, Reig M, Bruix J. Hepatocellular carcinoma. Lancet. 2018;391:1301–14. https://doi.org/10.1016/S0140-6736(18)30010-2.

3. Banerjee S, Wang DS, Kim HJ, Sirlin CB, Chan MG, Korn RL, et al. A computed tomography radiogenomic biomarker predicts microvascular invasion and clinical outcomes in hepatocellular carcinoma. Hepatology. 2015;62:792–800. https://doi.org/10.1002/hep.27877.

4. Bruix J, Gores GJ, Mazzaferro V. Hepatocellular carcinoma: clinical frontiers and perspectives. Gut. 2014;63:844–55. https://doi.org/10.1136/gutjnl-2013-306627.

5. Lin DC, Mayakonda A, Dinh HQ, Huang P, Lin L, Liu X, et al. Genomic and epigenomic heterogeneity of hepatocellular carcinoma. Cancer Res. 2017;77:2255–65. https://doi.org/10.1158/0008-5472.CAN-16-2822.

6. Lu LC, Hsu CH, Hsu C, Cheng AL. Tumor heterogeneity in hepatocellular carcinoma: facing the challenges. Liver Cancer. 2016;5:128–38. https://doi.org/10.1159/000367754.

7. Miyata R, Tanimoto A, Wakabayashi G, Shimazu M, Nakatsuka S, Mukai M, et al. Accuracy of preoperative prediction of microinvasion of portal vein in hepatocellular carcinoma using superparamagnetic iron oxide-enhanced magnetic resonance imaging and computed tomography during hepatic angiography. J Gastroenterol. 2006;41:987–95. https://doi.org/10.1007/s00535-006-1890-2.

8. Adachi E, Maeda T, Kajiyama K, Kinukawa N, Matsumata T, Sugimachi K, et al. Factors correlated with portal venous invasion by hepatocellular carcinoma: univariate and multivariate analyses of 232 resected cases without preoperative treatments. Cancer. 1996;77:2022–31. https://doi.org/10.1002/(SICI)1097-0142(19960515)77:10<2022::AID-CNCR9>3.0.CO;2-S.

9. Marsh JW, Dvorchik I, Bonham CA, Iwatsuki S. Is the pathologic TNM staging system for patients with hepatoma predictive of outcome? Cancer. 2000;88:538–43. https://doi.org/10.1002/(sici)1097-0142(20000201)88:3<538::aid-cncr7>3.0.co;2-h.

10. Jonas S, Bechstein WO, Steinmuller T, Herrmann M, Radke C, Berg T, et al. Vascular invasion and histopathologic grading determine outcome after liver transplantation for hepatocellular carcinoma in cirrhosis. Hepatology. 2001;33:1080–6. https://doi.org/10.1053/jhep.2001.23561.

11. Renzulli M, Brocchi S, Cucchetti A, Mazzotti F, Mosconi C, Sportoletti C, et al. Can current preoperative imaging be used to detect microvascular invasion of hepatocellular carcinoma? Radiology. 2016;279:432–42. https://doi.org/10.1148/radiol.2015150998.

12. Hu HT, Wang Z, Huang XW, Chen SL, Zheng X, Ruan SM, et al. Ultrasound-based radiomics score: a potential biomarker for the prediction of microvascular invasion in hepatocellular carcinoma. Eur Radiol. 2019;29:2890–901. https://doi.org/10.1007/s00330-018-5797-0.

13. Chandarana H, Robinson E, Hajdu CH, Drozhinin L, Babb JS, Taouli B. Microvascular invasion in hepatocellular carcinoma: is it predictable with pretransplant MRI? AJR Am J Roentgenol. 2011;196:1083–9. https://doi.org/10.2214/AJR.10.4720.

14. Lee JD, Yun M, Lee JM, Choi Y, Choi YH, Kim JS, et al. Analysis of gene expression profiles of hepatocellular carcinomas with regard to 18F-fluorodeoxyglucose uptake pattern on positron emission tomography. Eur J Nucl Med Mol Imaging. 2004;31:1621–30. https://doi.org/10.1007/s00259-004-1602-1.

15. Lee JD, Yang WI, Park YN, Kim KS, Choi JS, Yun M, et al. Different glucose uptake and glycolytic mechanisms between hepatocellular carcinoma and intrahepatic mass-forming cholangiocarcinoma with increased (18)F-FDG uptake. J Nucl Med. 2005;46:1753–9.

16. Li YC, Yang CS, Zhou WL, Li HS, Han YJ, Wang QS, et al. Low glucose metabolism in hepatocellular carcinoma with GPC3 expression. World J Gastroenterol. 2018;24:494–503. https://doi.org/10.3748/wjg.v24.i4.494.

17. Lim C, Salloum C, Chalaye J, Lahat E, Costentin CE, Osseis M, et al. 18F-FDG PET/CT predicts microvascular invasion and early recurrence after liver resection for hepatocellular carcinoma: a prospective observational study. HPB. 2019;21:739–47. https://doi.org/10.1016/j.hpb.2018.10.007.

18. Hyun SH, Eo JS, Song BI, Lee JW, Na SJ, Hong IK, et al. Preoperative prediction of microvascular invasion of hepatocellular carcinoma using (18)F-FDG PET/CT: a multicenter retrospective cohort study. Eur J Nucl Med Mol Imaging. 2018;45:720–6. https://doi.org/10.1007/s00259-017-3880-4.

19. Moon SH, Kim J, Joung JG, Cha H, Park WY, Ahn JS, et al. Correlations between metabolic texture features, genetic heterogeneity, and mutation burden in patients with lung cancer. Eur J Nucl Med Mol Imaging. 2019;46:446–54. https://doi.org/10.1007/s00259-018-4138-5.

20. Roayaie S, Blume IN, Thung SN, Guido M, Fiel MI, Hiotis S, et al. A system of classifying microvascular invasion to predict outcome after resection in patients with hepatocellular carcinoma. Gastroenterology. 2009;137:850–5. https://doi.org/10.1053/j.gastro.2009.06.003.

21. Xu X, Zhang HL, Liu QP, Sun SW, Zhang J, Zhu FP, et al. Radiomic analysis of contrast-enhanced CT predicts microvascular invasion and outcome in hepatocellular carcinoma. J Hepatol. 2019;70:1133–44. https://doi.org/10.1016/j.jhep.2019.02.023.

22. Nioche C, Orlhac F, Boughdad S, Reuze S, Goya-Outi J, Robert C, et al. LIFEx: a freeware for radiomic feature calculation in multimodality imaging to accelerate advances in the characterization of tumor heterogeneity. Cancer Res. 2018;78:4786–9. https://doi.org/10.1158/0008-5472.CAN-18-0125.

23. Sun R, Limkin EJ, Vakalopoulou M, Dercle L, Champiat S, Han SR, et al. A radiomics approach to assess tumour-infiltrating CD8 cells and response to anti-PD-1 or anti-PD-L1 immunotherapy: an imaging biomarker, retrospective multicohort study. Lancet Oncol. 2018;19:1180–91. https://doi.org/10.1016/S1470-2045(18)30413-3.

24. Camp RL, Dolled-Filhart M, Rimm DL. X-tile: a new bioinformatics tool for biomarker assessment and outcome-based cut-point optimization. Clin Cancer Res. 2004;10:7252–9. https://doi.org/10.1158/1078-0432.CCR-04-0713.

25. Mlynarsky L, Menachem Y, Shibolet O. Treatment of hepatocellular carcinoma: steps forward but still a long way to go. World J Hepatol. 2015;7:566–74. https://doi.org/10.4254/wjh.v7.i3.566.

26. Kobayashi T, Aikata H, Honda F, Nakano N, Nakamura Y, Hatooka M, et al. Preoperative fluorine 18 fluorodeoxyglucose positron emission tomography/computed tomography for prediction of microvascular invasion in small hepatocellular carcinoma. J Comput Assist Tomogr. 2016;40:524–30. https://doi.org/10.1097/RCT.0000000000000405.

27. Ahn SY, Lee JM, Joo I, Lee ES, Lee SJ, Cheon GJ, et al. Prediction of microvascular invasion of hepatocellular carcinoma using

gadoxetic acid-enhanced MR and (18)F-FDG PET/CT. Abdom Imaging. 2015;40:843–51. https://doi.org/10.1007/s00261-014-0256-0.

28. Cheung TT, Chan SC, Ho CL, Chok KS, Chan AC, Sharr WW, et al. Can positron emission tomography with the dual tracers [11 C]acetate and [18 F]fludeoxyglucose predict microvascular invasion in hepatocellular carcinoma? Liver Transpl. 2011;17:1218–25. https://doi.org/10.1002/lt.22362.

29. Ji GW, Zhu FP, Xu Q, Wang K, Wu MY, Tang WW, et al. Radiomic features at contrast-enhanced CT predict recurrence in early stage hepatocellular carcinoma: a multi-institutional study. Radiology. 2020;191470. https://doi.org/10.1148/radiol.2020191470.

30. Yang L, Gu D, Wei J, Yang C, Rao S, Wang W, et al. A radiomics nomogram for preoperative prediction of microvascular invasion in hepatocellular carcinoma. Liver Cancer. 2019;8:373–86. https://doi.org/10.1159/000494099.

31. De Angelis R, Sant M, Coleman MP, Francisci S, Baili P, Pierannunzio D, et al. Cancer survival in Europe 1999-2007 by country and age: results of EUROCARE–5-a population-based study. Lancet Oncol. 2014;15:23–34. https://doi.org/10.1016/S1470-2045(13)70546-1.

32. Fujiwara N, Friedman SL, Goossens N, Hoshida Y. Risk factors and prevention of hepatocellular carcinoma in the era of precision medicine. J Hepatol. 2018;68:526–49. https://doi.org/10.1016/j.jhep.2017.09.016.

33. Aerts HJ, Velazquez ER, Leijenaar RT, Parmar C, Grossmann P, Carvalho S, et al. Decoding tumour phenotype by noninvasive imaging using a quantitative radiomics approach. Nat Commun. 2014;5:4006. https://doi.org/10.1038/ncomms5006.

34. Jiang Y, Yuan Q, Lv W, Xi S, Huang W, Sun Z, et al. Radiomic signature of (18)F fluorodeoxyglucose PET/CT for prediction of gastric cancer survival and chemotherapeutic benefits. Theranostics. 2018;8:5915–28. https://doi.org/10.7150/thno.28018.

35. Kim JD, Cho EJ, Ahn C, Park SK, Choi JY, Lee HC, et al. A model to predict 1-month risk of transplant or death in hepatitis A-related acute liver failure. Hepatology. 2019;70:621–9. https://doi.org/10.1002/hep.30262.

36. Chen HS, Joo DJ, Shaheen M, Li Y, Wang Y, Yang J, et al. Randomized trial of spheroid reservoir bioartificial liver in porcine model of posthepatectomy liver failure. Hepatology. 2019;69:329–42. https://doi.org/10.1002/hep.30184.

37. Ampuero J, Jimeno C, Quiles R, Rosales JM, Llerena S, Palomo N, et al. Impact of comorbidities on patient outcomes after interferon-free therapy-induced viral eradication in hepatitis C. J Hepatol. 2018;68:940–8. https://doi.org/10.1016/j.jhep.2017.12.019.